Solid Earth
Discussions
Open Access

EGU

Crustal structure of southeast Australia from teleseismic receiver functions

Mohammed Bello[1,2], David G. Cornwell[1], Nicholas Rawlinson[3], Anya M. Reading[4], Othaniel K. Likkason[2]

[1]Department Geology & Geophysics, University of Aberdeen, Aberdeen, UK
[2]Department of Physics, Abubakar Tafawa Balewa University, Bauchi, Nigeria
[3]Department of Earth Sciences, University of Cambridge, UK
[4]School of Natural Sciences (Physics), University of Tasmania, Australia

Correspondence to: Mohammed Bello (mbazare13@yahoo.com)

Abstract. In an effort to improve our understanding of southeast Australia's enigmatic tectonic evolution, we analyse teleseismic earthquakes recorded by 24 temporary and 8 permanent broadband stations using the receiver function method. Crustal thickness, bulk seismic velocity and internal crustal structure of the southern Tasmanides – an assemblage of Palaeozoic accretionary orogens that occupy eastern Australia – are constrained by our new results which point to: (1) a 39.0 ± 0.5 km thick crust, a relatively high Poisson's ratio (0.262 ± 0.014) and a broad (>10 km) crust-mantle transition beneath the Lachlan Fold Belt. This is interpreted to represent magmatic underplating of mafic materials at the base of the crust; (2) a complex crustal structure beneath VanDieland, a postulated Precambrian continental fragment embedded in the southernmost Tasmanides, where the crust thickens (37.5 ± 1.2 km) towards the northern tip of the microcontinent as it enters south central Victoria but thins south into Bass Strait (30.5 ± 2.1 km), before once again becoming thicker beneath western Tasmania (33.5 ± 1.9 km). The thinner crust beneath Bass Strait can be attributed to lithospheric stretching that resulted from the break-up of Antarctica and Australia and the opening of the Tasman Sea; (3) stations located in the East Tasmania Terrane and eastern Bass Strait (ETT+EB) collectively indicate crust of uniform thickness (∼33 km) and a slightly broad Moho transition that reflect a possible underplating event associated with a Palaeozoic subduction system. The relative uniformity of V_P/V_S and Poisson's ratio in VanDieland – suggesting uniformity in composition – could be used in support of the VanDieland microcontinental model that explains the tectonic evolution of southeast Australia.

Keywords: receiver functions, crustal structure, VanDieland, Bass Strait, SE Australia

1 Introduction

The Phanerozoic Tasmanides (Collins and Vernon, 1994; Coney, 1995; Coney et al., 1990) comprise the eastern one-third of the Australian continent and through the process of subduction accretion were juxtaposed against the eastern flank of the Precambrian shield region of Australia beginning in the Late Neoproterozoic and Early Palaeozoic (Foster and Gray, 2000; Glen, 2005; Glen et al., 2009; Moresi et al., 2014) (Fig. 1). Persistent sources of debate that impede a more complete understanding of the geology of the Tasmanides include (1) the geological link between Tasmania – an island state in southeast Australia – and mainland Australia, which are separated by the waters of Bass Strait; and (2) the presence and locations of continental fragments from Rodinian remnants that are entrained within the accretionary orogens. Furthermore, the lateral boundaries between individual tectonic blocks and their crustal structure are often not well defined. To date, few constraints

Solid Earth

Discussions

Open Access

EGU

38   on crustal thickness and seismic velocity structure have been available for regions such as Bass Strait.

39   Constraints on the Moho transition, crustal thickness and velocity structure beneath Bass Strait derived from

40   receiver functions (RFs) can therefore provide fresh insight into the nature and evolution of the Tasmanides.

41   Previous estimates of crustal thickness and structure beneath southeastern Australia have been obtained from

42   deep seismic reflection transects, wide-angle seismic data, topography and gravity anomalies (e.g. Collins,

43   1991; Collins et al., 2003; Drummond et al., 2006; Kennett et al., 2011). Earlier RF studies in southeast

44   Australia (Shibutani et al., 1996; Clitheroe et al., 2000; Tkalčić et al., 2011; Fontaine et al., 2013a,b) suggested

45   the presence of complex lateral velocity variations in the mid-lower crust that probably reflect the interaction of

46   igneous underplating, associated thinning of the lithosphere, recent hotspot volcanism and uplift. Furthermore,

47   the intermediate to high crustal V_p/V_S ratio of 1.70–1.78 in this region (Fontaine et al., 2013a), relative to ak135

48   continental crust where V_p/V_S is ~1.68, may indicate a mafic composition that includes mafic granulite rocks,

49   granite-gneiss and biotite gneiss. Body- and surface-wave tomography (Fishwick and Rawlinson, 2012;

50   Rawlinson et al., 2015) reveal P and S wave velocity anomalies in the uppermost mantle beneath Bass Strait and

51   the Lachlan Fold Belt. Ambient noise surface wave tomography (Bodin et al., 2012b; Young et al., 2012; Pilia

52   et al., 2015b, 2016; Crowder et al., 2019) of the southern Tasmanides reveals significant crustal complexity, but

53   is unable to constrain crustal thickness or the nature of the Moho transition.

54   The goal of this paper is to provide fresh insight into the crust and Moho structure beneath the southern

55   Tasmanides using P-wave RFs, explain the origin of the lateral heterogeneities that are observed and explore the

56   geological relationship between the different tectonic units that constitute the southern Tasmanides, thereby

57   facilitating a better grasp of the region's tectonic history.

58   **2 Geological setting**

59   The Palaeozoic-Mesozoic Tasmanides of eastern Australia form part of one of the most extensive accretionary

60   orogens in existence and evolved from interaction between the East Gondwana margin and the Proto-Pacific

61   Ocean. The tectonic evolution of the Tasmanides is complex and large-scale reconstructions have proven

62   difficult. This is evident from the variety of models that have been suggested to explain how the region formed

63   (Foster and Gray, 2000; Spaggiari et al., 2003; Teasdale et al., 2003; Spaggiari et al., 2004; Boger and Miller,

64   2004; Glen, 2005; Cawood, 2005; Glen et al., 2009; Cayley, 2011; Gibson et al., 2011; Moresi et al., 2014; Pilia

65   et al., 2015a,b). Particular challenges arise from multiple subduction events, multiple phases of metamorphism,

66   entrainment of exotic continental blocks, the formation of large oroclines, recent intraplate volcanism and

67   subsequent events, including the separation of Antarctica and Australia and the formation of the Tasman Sea.

68   These challenges are compounded by the presence of widespread sedimentary sequences that hinder direct

69   access to basement rocks (Fig. 1).

70   The Tasmanides consist of four orogenic belts, namely the Delamerian, Lachlan, Thomson and New England

71   Orogens. The Delamerian Orogen - located in the south - is the oldest part of the Tasmanides and has a

72   southward extension across Bass Strait from Victoria into western Tasmania, where it is commonly referred to

73   as the Tyennan Orogen (Berry et al., 2008). Between about 514 and 490 Ma, the Precambrian and Early

74   Cambrian rocks that constitute the Delamerian Orogen were subjected to contractional orogenic event along the

75 margin of East Gondwana (Foden et al., 2006). Subsequently, the Lachlan Orogen formed in the east, which

76 contains rocks that vary in age from Ordovician to Carboniferous (Glen, 2005). Gray and Foster (2004) argued

77 for a tectonic model for the Lachlan Orogen that involved interaction of a volcanic arc, oceanic microplates,

78 several turbidite thrust systems and three distinct subduction zones. Each subduction zones is linked to the

79 formation of distinct tectonic terrain: the Stawell-Bendigo zone, Tabbarebbera zone and Narooma accretionary

80 complex. The limited rock exposure in the Tasmanides as a whole has made direct observation of the Lachlan

81 Orogen difficult; this is attributed to a large swath of Mesozoic-Cenozoic sedimentary cover and more recent

82 Quaternary volcanics which obscure a large portion of the underlying Palaeozoic terrane. However, the Lachlan

83 Orogen contain belts of Cambrian rocks in Victoria and New South Wales that are similar in age to the

84 Delamerian Orogen (Gray and Foster, 2004).

85 The presence of Precambrian outcrops in Tasmania and the relative lack of similar age rocks in adjacent

86 mainland Australia has led to different models which attempted to explain the existence of Proterozoic

87 Tasmania. For instance, Li et al. (1997) suggested that western Tasmania may be a remnant of a continental

88 fragment set adrift by Rodianian break-up, whereas Calvert and Walter (2000) proposed that King Island, along

89 with western Tasmania, rifted away from the Australian craton around ~600 Ma (Fig. 1). Other researchers have

90 developed scenarios in which the island of Tasmania was present as a separate microcontinental block that was

91 positioned outboard of the eastern margin of Gondwana before re-attaching at the commencement of the

92 Palaeozoic (Berry et al., 2008).

93 A popular model that attempts to reconcile the geology observed in Tasmania and adjacent mainland Australia

94 is that of Cayley (2011). This model proposes that central Victoria and western Tasmania formed a

95 microcontinental block called "VanDieland" that fused with East Gondwana at the end of the Cambrian,

96 possibly terminating the Delamerian Orogeny. VanDieland became entangled in the subduction-accretion

97 system that built the Palaeozoic orogens that now comprise eastern Australia (Fig. 1). Delineating Precambrian

98 continental fragments within southeast Australia has proven difficult partly due to more recent sedimentary

99 cover that obscures large tracts of the Tasmanides. However, if present, they likely have distinctive structural

100 and seismic velocity characteristics.

101 **3 Previous geophysical studies**

102 Imaging techniques previously employed to study crustal structure beneath the Tasmanides include: RF analysis

103 (e.g. Shibutani et al., 1996; Clitheroe et al., 2000; Chevrot and van der Hilst, 2000; Kennett et al., 2011;

104 Fontaine et al., 2013a,b), ambient noise tomography (e.g. Saygin and Kennett, 2010; Bodin et al., 2012b; Young

105 et al., 2013a,b; Pilia et al., 2015a,b; Crowder et al., 2019), studies based on potential field imaging and

106 numerical modelling (e.g. Gunn et al., 1997; Morse et al., 2009; Moresi et al., 2014; Moore et al., 2015, 2016),

107 teleseismic tomography (Rawlinson and Urvoy, 2006; Rawlinson and Kennett, 2008; Rawlinson et al., 2015,

108 2016; Bello et al., 2019b) and seismic reflection and refraction profiling (e.g. Finlayson et al., 1980; Collins,

109 1991; Direen et al., 2001; Glen et al., 2002; Finlayson et al., 2002; Drummond et al., 2006; Cayley et al., 2011;

110 Glen, 2013). The work of Clitheroe et al. (2000) used RFs to map broad-scale crustal thickness and Moho

111 character across the Australian continent. These findings confirmed the previous work of Drummond and

112 Collins (1986) and Collins (1991) who used seismic reflection and refraction transects to determine that the

113   Lachlan Fold Belt has the thickest crust (~50 km) in eastern Australia. Shibutani et al. (1996) applied a genetic
114   algorithm inversion, a non-linear global optimisation technique, to determine the lithospheric velocity structure
115   of southeast Australia from teleseismic RFs. They found that the Moho is shallow (30-36 km) and sharp within
116   the craton and deep (38-44 km) and transitional beneath the Tasmanides. They suggested that underplating or
117   intrusion of mantle material may have thickened the crust and produced a less distinct contrast across the Moho.
118   A more recent study by Fontaine et al. (2013a) employed $H\text{-}\kappa$ stacking and non-linear RF inversion to
119   investigate crustal thickness, shear wave velocity structure, as well as dipping and anisotropy of the crustal
120   layers. Their results also indicated a thick crust (~48 km) and an intermediate (2-9 km) crust-mantle transition
121   beneath the Lachlan Fold Belt zone which could be attributed to underplating beneath the crust and/or high
122   concentrations of mafic rocks in the mid-lower crust. Their results also showed a dipping Moho together with
123   crustal anisotropy in the vicinity of three seismic stations (YNG, CNB and CAN). In our new work, we have a
124   much increased data coverage of the study area (southern Tasmanides); this allows us to resolve new features,
125   and further investigate the presence of structures that have been suggested by previous studies.

126   Over the last decade, ambient noise tomography has become popular tool for studying the structure of the
127   Australian crust. Saygin and Kennett (2010) produced the first group velocity maps of the Australian continent
128   from Rayleigh wave group velocity dispersion in the period range 5.0–12.5 seconds. Limited spatial resolution
129   ($\sim 2^\circ$ x 2°) in our study region means that this model is only able to represent the structure beneath Bass Strait
130   as a broad, low velocity anomaly. However, the group velocities exhibit a good correlation with known basins
131   and cratons. Subsequent studies using denser arrays covering southeast mainland Australia (Arroucau et al.,
132   2010) and northern Tasmania (Young et al., 2011) show good correlations between group/phase velocity maps
133   and sedimentary and basement terrane boundaries. In order to account for uneven data distribution, Bodin et al.
134   (2012b) used a Bayesian transdimensional inversion scheme to generate group velocity maps that span the
135   Australian continent from multi-scale ambient noise datasets. However, in our study area their model is of low
136   resolution due to the limited station coverage and hence few details on crustal structure can be inferred. Bodin et
137   al. (2012a) subsequently applied Bayesian statistics to reconstruct the Moho depth of Australia using a variety
138   of seismic datasets, which gave an approximate Moho depth of ~30 km beneath Bass Strait.

139   Potential field data have also been exploited to study the formation and structure of the Tasmanides. Gunn et al.
140   (1997) integrated potential field data (magnetic and gravity), seismic reflection data, outcrop geology and well
141   information to study the crustal structure of the Australian continent. Their study found that the occurrence of
142   tensional stress oriented NE-SW along basement structures in the Bass Basin is able to explain the formation of
143   the three major sedimentary basins that overlie dense mafic material, which in turn was formed by mantle
144   decompression processes associated with crustal stretching. From the interpretation of new aeromagnetic data,
145   Morse et al. (2009) delineated the architecture of the Bass Strait basins and their supporting basement structure.
146   Subsequent studies by Moore et al. (2015, 2016) used gravity, magnetic, seismic reflection and outcrop data to
147   support the hypothesis of a VanDieland microcontinent. Their study showed that VanDieland comprises seven
148   distinct microcontinental ribbon terranes that appear to have amalgamated by the Late Cambrian with major
149   faults and suture zones bonding these ribbon terranes together.

150   While the last few decades has seen important advances and insights made into our understanding of the

151 southern Tasmanides, there still remains limited data on the deep crustal structure beneath Bass Strait, which is

152 our region of interest. It is therefore timely that can exploit, using the RF technique, teleseismic data recorded

153 by a collection of temporary and permanent seismic stations in the region to study the structure of the crust,

154 Moho and uppermost mantle beneath mainland Australia, Bass Strait and Tasmania.

155 **4 Data**

156 A collaboration involving five organisations (University of Tasmania, Australian National University, Mineral

157 Resources Tasmania, the Geological Survey of Victoria and FROGTECH) deployed the temporary Bass seismic

158 array from May 2011 to April 2013. It consisted of 24 broadband, three-component seismic stations that

159 spanned northern Tasmania, a selection of islands in Bass Strait and southern Victoria. The instruments used

160 were 23 Güralp 40T and one Güralp 3ESP sensors coupled to Earth Data PR6-24 data loggers. The permanent

161 stations consist of eight broadband sensors managed by IRIS, GEOSCOPE and the Australian National Seismic

162 Network (ANSN). The distribution of all 32 seismic stations that are used in this study is plotted in Fig. 2.

163 Earthquakes with magnitudes m_b > 5.5 at epicentral distances between $30°$ and $90°$ comprise the seismic

164 sources used in this analysis (Fig. 3). This resulted in an acceptable azimuthal coverage of earthquakes between

165 the northwest and east of the array, where active convergence of the Australian and Eurasian plate coupled with

166 westward motion of the Pacific plate has produced extensive subduction zones. To the south and southwest of

167 the array, the absence of subduction zones in the required epicentral distance range means that there are

168 significantly fewer events available for analysis from these regions.

169 **5 Methods**

170 **5.1 Receiver functions**

171 The RF technique (Langston, 1979) uses earthquakes at teleseismic distances to enable estimation of Moho

172 depth and shear wave velocity structure in the neighbourhood of a seismic recorder. If this technique can be

173 applied to a network of stations with good spatial coverage, it represents an effective way of mapping lateral

174 variations in Moho depth and crustal structure. The coverage and quality of broadband data available for this

175 study provides a sound basis on which to examine the crustal structure of the southern Tasmanides.

176 A recorded teleseismic wavefield at a broadband station can be described by the convolutional model in which

177 operators that represent the source radiation pattern, path effects, crustal structure below the station and

178 instrument response are combined to describe the recorded waveform. By using deconvolution to remove the

179 effects of the source, path and response of the instrument (e.g. Langston, 1979), information on local crustal

180 structure beneath the station can be extracted from P - to S -wave conversions at discontinuities in seismic

181 velocity (Owens et al., 1987; Ammon, 1991).

182 *P*-wave RFs were determined from teleseismic *P*-waveforms using FuncLab software (Eagar and Fouch, 2012;

183 Porritt and Miller, 2018), following preprocessing using the seismic analysis code (SAC) (Goldstein et al.,

184 2003). The complete set of 1765 events (Fig. 3) and 32 stations produced 21,671 preliminary RFs. These RFs

185 were manually picked using the FuncLab trace editor, and by using the clarity of the direct arrivals as an

186 acceptance criteria, a total of 9,674 RFs were retained for further analysis. The RFs were computed using an

Solid Earth

Discussions

Open Access

EGU

187   iterative time-domain deconvolution scheme developed by Ligorria and Ammon, 1999 with a 2.5 s Gaussian

188   filter width. This is performed by deconvolution of the vertical component waveform from the radial and

189   transverse waveforms with a central frequency of 1 Hz. This frequency was selected on account of significant

190   source energy detected in the 1 Hz range of teleseismic P arrivals, which are sensitive to crustal-scale

191   anomalies. It also provides a favourable lateral sensitivity with respect to Fresnel zone width (∼15 km at Moho

192   depth) when the conversions from P to S are mapped as velocity and crustal thickness variations.

193   **5.2 H-κ stacking**

194   Having obtained reliable P-wave RFs, the H-κ stacking technique is used to estimate crustal thickness,

195   Poisson's ratio and bulk V_p/V_s. We apply the method of Zhu and Kanamori (2000) to stations where the direct

196   P_S (Moho P-to-S conversion) and its multiples are observed. This technique makes use of a grid search to

197   determine the crustal thickness (H) and V_p/V_s (κ) values that correspond to the peak amplitude of the stacked

198   phases. A clear maximum requires a contribution from both the primary phase (P_S) and the associated multiples

199   (P_pP_S and P_pS_S +P_SP_S). In the absence of multiples, the maximum becomes smeared out due to the inherent

200   trade-off between crustal thickness (H) and average crustal velocity properties (κ) (Ammon et al., 1990; Zhu and

201   Kanamori, 2000). The H-κ stacking algorithm reduces the aforementioned ambiguity by summing RF

202   amplitudes for P_S and its multiples P_pP_S and P_pS_S +P_SP_S at arrival times corresponding to a range of H and

203   V_p/V_s values. In the H-κ domain the equation for stacking amplitude

$$s(H,K) = \sum_{j=1}^{N} w_1 r_j(t_1) + w_2 r_j(t_2) - w_3 r_j(t_3) \qquad (1)$$

204   where $r_j(t_j); i = 1,2,3$ are the RF amplitude values at the expected arrival times $t_1, t_2,$ and t_3 of the Ps, $PpPs$,

205   $PpSs$ +$PsPs$ phases respectively for the jth RF, w_1, w_2, w_3 are weights based on the signal to noise ratio

206   ($w_1 + w_2 + w_3 = 1$), and N is the total number of radial RFs for the station. s(H,κ) achieves its maximum value

207   when all three phases stack constructively, thereby producing estimates for H and Vp/Vs beneath the station. In

208   this study, the weighting factors used are $w_1 = 0.6, w_2 = 0.3$ and $w_3 = 0.1$ (Zhu and Kanamori, 2000). The H-κ

209   approach requires an estimate of the mean crustal P-wave velocity, which is used as an initial value. Based on

210   the results of a previous seismic refraction study (Drummond and Collins, 1986), we use an average crustal

211   velocity of Vp = 6.65 km/s to obtain our estimates of H and κ in the study area, noting that H-κ stacking results

212   are much more dependent on Vp/Vs than Vp (Zhu and Kanamori, 2000). To estimate the uncertainties in the H-κ

213   stacking results, we compute the standard deviation of the H and κ values at each station.

214   H-κ stacking can also be used to determine Poisson's ratio, which is a useful parameter for inferring the physical

215   and compositional properties of the crust (Christensen, 1996) and providing insight into fractures, fluids, and

216   partial melt (e.g. Mavko, 1980). The Poisson's ratio σ can be determined from κ using the equation

$$\sigma = \frac{1}{2}\left(1 - \frac{1}{\kappa^2 - 1}\right) \qquad (2)$$

217   where $\kappa = Vp/V_S$. While simple to implement, the Zhu and Kanamori (2000) method can suffer from large

218   uncertainties due to its assumption of a simple flat-laying layer over half-space with constant crustal and upper

219   mantle properties. Consequently, there are only two search parameters (H and κ) plus *a priori* information (V_p,

220   weightings) and it does not account for variation with backazimuth. These problems can cause non-unique and

221   inaccurate estimates, which can lead to potentially misleading interpretations; for instance a low velocity upper

222   crustal layer can appear as a very shallow Moho in an *H-κ* stacking search space diagram. Also, a dipping Moho

223   and/or anisotropic layers within the crust can contribute to uncertainty.

5.3 Nonlinear waveform inversion

225   In an effort to refine the crustal model, we invert a stack of the radial RFs by adopting the workflow described

226   by Shibutani et al. (1996). We divide the waveform data (RFs) into four 90° quadrants based on the backazimuth

227   of their incoming energy. The 1st quadrant backazimuth range is from 0° and 90°, and an equivalent range in a

228   clockwise direction defines the consecutive quadrants. The 2nd and 3rd quadrants (south-eastern and south-

229   western backazimuths) have very small numbers of RFs. Data from the 1st and 4th quadrants are of better quality,

230   with the 1st quadrant showing more coherency than the 4th quadrant, which is likely due to the orientation of

231   surrounding tectonic plate boundaries and hence the pattern of *P*-wave energy radiated towards Australia.

232   Kennett and Furumura (2008) showed that seismic waves arriving in Australia from the northern azimuths

233   undergo multiple scattering but low intrinsic attenuation due to heterogeneity in the lower crust and mantle; this

234   tends to produce prolonged high-frequency coda. An important assumption in our inversion is that we neglect

235   anisotropy and possible Moho dip, which we assume have a second order influence on the waveforms we use to

236   constrain 1-D models of the crust and upper mantle.

237   Visual examination of coherency in *P* to *S* conversions allows us to select a subset of RF waveforms for

238   subsequent stacking. This resulted in groups of mutually coherent waveforms after which a moveout correction

239   is then applied to remove the kinematic effect of different earthquake distances prior to stacking using a cross-

240   correlation matrix approach described in Chen et al. (2010) and Tkalčić et al. (2011). Our strict criteria give

241   reliable RFs at only 6 out of the 32 stations used for this study. An example of some stacked RFs is given in Fig.

242   4.

5.3.1 Neighborhood algorithm

244   We invert RFs for 1-D seismic velocity structure beneath selected seismic stations using the Neighbourhood

245   Algorithm or NA (Sambridge, 1999a,b) in order to better understand the internal structure of the crust and the

246   nature of the transition to the upper mantle. NA makes use of Voronoi cells to help construct a searchable

247   parameter space, with the aim of preferentially sampling regions of low data misfit. In the inversion process, a

248   Thomson-Haskell matrix method (Thomson, 1950 and Haskell, 1953) was used to calculate a synthetic radial

249   RF for a given 1-D (layered) structure. During the inversion, as in Shibutani et al. (1996) and Clitheroe et al.

250   (2000), each model is described by six layers: a layer of sediment, a basement layer, an upper crust, middle crust

251   and lower crust, and an underlying mantle layer, all of which feature velocity gradients and potentially, velocity

252   jumps across boundaries. The inversion involves constraining 24 parameters: *Vs* values at the top and bottom of

253   each layer, layer thickness and the *Vp/Vs* ratio in each layer (Table 1). The inclusion of *Vp/Vs* ratio as an

254   unknown primarily aims to accommodate the effects of a sediment layer with limited prior constraints

255   (Bannister et al., 2003). There are two important controlling parameters required by NA: (1) the number of

256   models produced per iteration (n_s); and (2) the number of neighbourhoods re-sampled per iteration (n_r). After a

257   number of trials we chose the maximum number of iterations to be 5500, with $n_s = 13$ and $n_r = 13$ for all

258   iterations. We employ a chi-squared (χ^2) metric to compute the misfit function, which is a measure of the

259   inconsistency between the true $\emptyset_i^{obs}(m)$, and predicted, $\emptyset_i^{pre}(m)$ waveforms for a given model (m):

$$\chi_v^2(m) = \frac{1}{v}\sum_{i=1}^{N_d}\left(\frac{\emptyset_i^{obs} - \emptyset_i^{pre}}{\sigma_i}\right)^2 \tag{3}$$

260   where σ_i represents the noise standard deviation determined from $\emptyset_i^{obs}$, as explained by Gouveia and Scales

261   (1998), and v represents the number of degrees of freedom. Using the above stated parameters, the inversion

262   targets the 1-D structure that produces the best fit between the predicted and observed RF. Figure 7 and 8

263   present example results of inversions via density plots of the best 1000 data-fitting S-wave velocity models

264   produced by the NA. The optimum data-fitting model is plotted in red.

265   6 Results

266   6.1 *H-κ* stacking results for Moho depth and Vp/Vs (including Poisson's ratio)

267   Maps depicting crustal thicknesses and average Vp/Vs in southeast Australia are plotted from the results

268   obtained at 14 stations (Fig. 6 and 9). At the remaining stations, we could not detect any clear multiples or

269   Moho conversions in the RFs from any direction. A previous study by Chevrot and van der Hilst (2000) has

270   noted that this region is devoid of clear multiples. The crustal thickness for all analysed stations in the study

271   area varies from 30.0 ± 2.1 km (BA11) beneath King island in Bass Strait to 39.1 ± 0.5 km (CAN) beneath the

272   Lachlan Fold Belt, and the variation strongly correlates with topography. The associated Vp/Vs values range

273   from 1.65 ± 0.07 (BA11) beneath King island to 1.76 ± 0.04 (YNG) beneath the Lachlan Fold Belt. Crust of the

274   order of 30–34 km thickness occurs beneath much of VanDieland. The mountainous region of the Lachlan Fold

275   Belt has the deepest Moho at 39.1 ± 0.5 km (CAN) and a corresponding Vp/Vs value of 1.73 ± 0.02. Crust that is

276   ~33 km thick lies beneath the East Tasmania Terrane and Eastern Bass Strait (ETT+EB). Table 2 is a summary

277   of *H-κ* stacking parameters for the analysed stations.

278   At ~40 km, the crustal thickness beneath the Lachlan Fold Belt is significant, but decreases southward towards

279   VanDieland (~32.5 km) and southeastward towards the East Tasmania Terrane and Eastern Bass Strait

280   (ETT+EB) (~33 km). Overall, the Moho becomes shallower from the southern tip of VanDieland (TAU)

281   towards and into Bass Strait to the north, before becoming deeper once more under the mainland part of the

282   VanDieland microcontinental block (Fig. 6a). The crustal thickness is more or less uniform beneath the Lachlan

283   Fold Belt, East Tasmania Terrane and eastern Bass Strait.

284   The majority of our study region has a low-to-intermediate Poisson's ratio. Poisson's ratio is highest (0.262 ±

285   0.014) in the Lachlan Fold Belt (see Table 2). In VanDieland, the Poisson's ratios generally decrease northward

286   into Bass Strait from 0.240 ± 0.019 (MOO) to 0.210 ± 0.013 (BA11) and then increase into mainland Australia

287   to 0.226 ± 0.017 (TOO). The relatively average to high values in the Lachlan Fold Belt (0.235 ± 0.017 – 0.262 ±

288   0.014) are in agreement with the presence of a mafic lower crust, as suggested by a number of other studies

289   (Drummond and Collins, 1986; Shibutani et al., 1996; Clitheroe et al., 2000; Finlayson et al., 2002). The ratios

290   in the ETT+EB (0.220 ± 0.008 (BA08) – 0.242 ± 0.005 (BA17)) agree with constraints from seismic reflection

291   and refraction studies and may indicate a felsic to intermediate (average) crustal composition (Finlayson et al.,

292   2002; Collins et al., 2003).

6.2 Nonlinear inversion results

294   Results of the NA inversion were successfully obtained for a selection of stations, as shown in Table 2. If the

295   Moho is defined by a gentle velocity gradient, the base of the velocity gradient is used as a proxy for the Moho

296   depth, as done in previous RF (e.g. Clitheroe et al., 2000; Fontaine et al., 2013a) and seismic refraction

297   (Collins, 1991; Collins et al., 2003) studies. We also adopt an upper mantle velocity of Vp = 7.6 km/s (i.e. Vs =

298   4.3-4.4 km/s for Vp/Vs ratios of 1.73-1.77 at the base of the Moho gradient) following Clitheroe et al. (2000)

299   who used this value for RF studies, and Collins et al. (2003) who used Vp > 7.8 km/s for their summary of both

300   seismic refraction and RF results; these Vp values are consistent with global Earth models. Therefore, we also

301   require the S-wave velocity to be > 4.4 km/s beneath the Moho. We present the S-wave velocity profiles from

302   the NA inversion for stations CAN, MOO, TOO and YNG in Figs. 7 and 8, together with observed and

303   predicted RFs. The S-wave velocity inversion results of the remaining two stations are included as

304   supplementary material (see Fig. S.10). In assigning the Moho depth, we consider three criteria to examine the

305   quality of the inversion result: (1) misfit value (χ^2); (2) the quality of the RF stack (which is based on our

306   ability to pick the direct and multiple phases); and (3) the visual fit between the synthetic and observed RF.

307   Models that fail to fit significant arrivals in the observed RF are rejected. Based on these criteria, the inversion

308   results are classified as:

309   •   Very good: very low χ^2 (typically < 0.4), very good visual fit to direct and multiple phases.

310   •   Good: low χ^2 (typically 0.4-0.8), direct phases clearly visible, multiple phases less clear, and a good

311   visual fit to all major identifiable phases.

312   •   Poor: medium to high χ^2 (in the range 0.8-1.2), direct phases visible, multiple phases unclear, and

313   moderate visual fit to some identifiable phases. Looking at the character of the crust-mantle transition,

314   this study classifies the transition zone as sharp ≤ 2 km, intermediate 2-10 km or broad ≥ 10 km as

315   initially proposed by Shibutani et al. (1996) and modified by Clitheroe et al. (2000).

7 Discussion

317   For convenience, the seismic stations were separated into three groups (Fig. 2 and Table 2) based on tectonic

318   settings and the results obtained. Stations YNG, CAN, CNB, MILA and BA13 are located in the Lachlan Fold

319   Belt; stations BA02, BA11, TAU, MOO and TOO sit above the VanDieland microcontinental block; and

320   stations BA07, BA08 and BA17 lie in the East Tasmania Terrane and Eastern Bass Strait (ETT+EB). This

321   discussion focuses on crustal thickness and the nature of the Moho from H-κ stacking and the nature of the crust

322   from *Vp/Vs*, Poisson's ratio and the 1-D *S*-wave velocity models.

7.1 Lateral variation of crustal thickness and nature of the Moho

324   The RF analysis clearly reveals the presence of lateral changes in crustal thickness that span mainland Australia

325   through Bass Strait to Tasmania. The stations located in the Palaeozoic Lachlan Fold Belt reveals a generally

326   thick crust that ranges from 36.5 ± 4.4 to 39.1 ± 0.5 km. At station CAN, there is a disparity in crustal thickness

327   obtained by the non-linear inversion method (~49 km) and *H-κ* stacking technique (39.1 ± 0.5 km). The reason

328   appears to be that the *H-κ* stacking analysis assumes that the crust is a single layer with a velocity jump across

329   the Moho, whereas the crust-mantle transition is actually gradual; hence it instead targets a shallower boundary

330   that is not the Moho. Therefore, the deep crustal structure obtained at YNG, CAN and CNB is part of a broad

331   velocity transition zone from crust to mantle. The crustal thickness and Moho transition zone beneath the

332   Lachlan Orogen obtained by the nonlinear inversion method is consistent with previous refraction and RF

333   studies (Shibutani et al., 1996; Clitheroe et al., 2000; Collins et al., 2003; Fontaine et al., 2013a,b). The crustal

334   thickness variations and lack of a clear Moho at the base of the Lachlan Orogen crust may be a consequence of

335   mafic magmatic underplating (e.g. Drummond and Collins, 1986; Shibutani et al., 1996; Clitheroe et al., 2000),

336   sourced from the ambient convecting mantle. This reinforces the opinion of Glen et al. (2002), who suggested

337   that the deep Moho underlying the Lachlan Orogen results from magmatic underplating that added a thick

338   Ordovician mafic layer at the base of the crust coupled with a thick sequence of Ordovician mafic rocks that can

339   be found in the mid and lower crust. Finlayson et al. (2002) and Glen et al. (2002) also inferred the presence of

340   underplating near CNB and CAN from seismic refraction data. Collins (2002) postulated that the underplating

341   might have occurred in the back-arc region of a subduction zone due to pronounced adiabatic decompression

342   melting in the asthenosphere. The seismic tomography model of Rawlinson et al. (2010, 2011) exhibits an

343   increase in *P*-wavespeed at 50 km depth beneath CAN, CNB and YNG and the authors suggest that magmatic

344   underplating may be the cause of the high velocity anomaly. A recent study by Davies et al. (2015) identified

345   the longest continental hotspot track in the world (over 2000 km total length), which began in north Queensland

346   at ~33 Ma, and propagated southward underneath the present day Lachlan Fold Belt and Bass Strait. The

347   magmatic underplating could therefore be a consequence of the passage of the continent above a mantle

348   upwelling leading to a more diffuse crust-mantle transition zone. The thickened crust and a transitional Moho

349   observed in the Lachlan Fold Belt are consistent with the proposed delamination models of Collins and Vernon

350   (1994).

351   Strong lateral changes in crustal structure and/or composition beneath VanDieland appear to be a reflection of

352   the region's complex tectonic history (Fig. 6 and 9). The thick crust (37.5 ± 1.2 km) beneath the Selwyn Block –

353   within the northern margin of VanDieland in southern Victoria – thins (to 30.5 ± 2.1 km) as it enters Bass Strait,

354   yet in southern Tasmania, at stations TAU and MOO, the crust is thicker (33.5 ± 1.9 km). This is reflected in

355   both the NA inversion and *H-κ* stacking depth estimates where a sharp Moho is observed beneath this region of

356   the study area (Fig. 6 and 9). The Moho depth estimates from RFs at stations TAU and MOO (~34 km) is

357   almost identical (~35 km) to that deduced by Korsch et al. (2002) from a seismic reflection profile adjacent to

358   the two seismic stations. In contrast, the Bass Strait portion of VanDieland appears to have a relatively thinner

359   crust (~30 km). This may indicate thinning of the lithosphere associated with lithospheric stretching and or

360   delamination that resulted from tectonic events that occur post-formation of the Tasmanides (Gaina et al., 1998).

361   Stations BA07, BA08 and BA17 (ETT+EB) collectively indicate crust of uniform thickness (~33 km, Figures
362   9a,b). Relative to western Bass Strait, the crust thickens slightly in this part of the study area, which may
363   suggest underplating associated with a Palaeozoic subduction system (e.g. Drummond and Collins, 1986; Gray
364   and Foster, 2004). Furthermore, our results support the crustal thickness estimates of Tasmania from refraction
365   and wide-angle reflection travel time tomography by Rawlinson et al. (2001). They suggested that the
366   thickening of the crust beneath central northern Tasmania is associated with the suturing of the West and East
367   Tasmania Terranes during the Middle Devonian Tabberabberan Orogeny. The Moho depths we obtained at
368   stations TAU, MOO, BA02 and BA11 which are located within their study area show significant overlap in
369   crustal thickness estimates (Fig. S10 in supplementary material).

370   In general, our understanding of crustal thicknesses variations are limited by station separation, so it is difficult
371   to determine whether smooth variations in thickness or step-like transitions explain the observations.

372   **7.2 Poisson's ratio, V_p/V_S and average crustal composition**

373   Poisson's ratio, which shares an inverse squared relationship to Vp/Vs (Eq. 2) can constrain chemical
374   composition and mineralogy more robustly than P- or S-wave velocity in isolation (Christensen and Fountain,
375   1975). We observe variations in Poisson's ratio (and hence Vp/Vs) across the study region, which we equate
376   with variations in composition. Studies in mineral physics and field observations show (1) a linear increase in
377   Poisson's ratio with decreasing SiO_2 content in the continental crust and (2) partial melt is depicted by an
378   elevated Poisson's ratio (>0.30), especially if the anomaly is localised to an intra-crustal layer (Owens and
379   Zandt, 1997). In terms of Vp/Vs, a more felsic (SiO_2) composition in the lower crust is represented by a lower
380   Vp/Vs, which reflects removal of an intermediate-mafic zone by delamination, whereas a more mafic lower crust
381   is depicted by higher Vp/Vs (> 1.75) which may be due to underplated material (Pan and Niu, 2011). However,
382   lower crustal delamination can also result in decompression melting, which can yield elevated Vp/Vs (He et al.,
383   2015). We interpret the variation of observed Poisson's ratios (0.210–0.256) in the southern Tasmanides to be a
384   consequence of compositionally heterogeneous crust and localised partial melt that may likely be sourced from
385   recent intraplate volcanism (Rawlinson et al., 2017).

386   Figure 6b shows the distribution of bulk Vp/Vs across the study area. Upon comparison with our Moho depth
387   results (Fig. 6a and 9a,b), we find that areas of thick crust (Lachlan Fold Belt) do overlap with areas of higher
388   Vp/Vs (1.70 ± 0.04 − 1.76 ± 0.04). This may strengthen the argument for mafic magmatic underplating sourced
389   from an ambient convecting mantle (Glen et al., 2002). At MILA, BA13, CAN and CNB, the Vp/Vs values (1.70
390   ± 0.04–1.73 ± 0.06) are consistent with mafic granulite (Christensen and Fountain, 1975) which has been
391   suggested to occur in the lower crust based on a wide-angle seismic line that cross-cuts the southern region of
392   the Lachlan Orogen (Finlayson et al., 2002). At station YNG the Vp/Vs value of 1.76 ± 0.04 is consistent with
393   biotite gneisses deduced from seismic reflection experiments carried out across the Junee-Narromine Volcanic
394   Belt in the neighborhood of YNG (Direen et al., 2001).

395   The VanDieland Vp/Vs distribution is rather complex, hence we further divide this block into two separate

396   groups: (1) West Tasmania Terrane (WTT); (2) and the Selwyn block. In the WTT, stations BA02, TAU, MOO

397   (see Fig. 2 for the location) have a moderate Vp/Vs (1.69 ± 0.02–1.71 ± 0.04). The bulk Vp/Vs beneath BA02

398   (1.69 ± 0.02) supports a dominantly felsic crustal composition, which means that it is unlikely that the WTT has

399   a mafic lower crust. A felsic crustal composition is at odds with the crustal composition required by the lower

400   crustal flow model of Drummond and Collins (1986); Gray and Foster (2004). Our Vp/Vs measurement from the

401   permanent GSN station TAU (1.70 ± 0.08), agrees well with Vp/Vs value at BA02 which implies a similar

402   crustal composition. Station MOO adjacent to TAU exhibits a similar Vp/Vs value (1.71 ± 0.04) and together

403   this may indicate that the crust is more or less homogeneous in this region. However, the slight variation in

404   Vp/Vs values between station MOO and TAU may be associated with a slight change in bulk composition and

405   the effects of heating following juxtaposition of western and eastern Tasmania during the Middle Devonian

406   Tabberabberan Orogeny.

407   In Bass Strait and south central Victoria (underlain in part by the Selwyn Block), the abrupt variations in Vp/Vs

408   values across stations BA11 and TOO help to underscore the region's complex tectonic evolution. Very few

409   reliable H-κ stacking parameters were observed in this region: one on King Island (BA11) and the other

410   adjacent to the NVP in south central Victoria. This is attributed to low signal quality/difficulty in identifying

411   crustal multiples in this region (Chevrot and van der Hilst, 2000). The presence of a complex and

412   compositionally variable Selwyn Block beneath the stations (Cayley et al., 2002), and melt-induced heating of

413   the crust associated with the Quaternary NVP, may also be contributing factors. The Vp/Vs value at BA11 (1.65

414   ± 0.07) is the lowest in the study area which may imply a lower crustal delamination in Bass Strait, leaving a

415   dominantly felsic crust (e.g. He et al., 2015; Bello et al., 2019b).

416   Station TOO located adjacent to the NVP exhibits a relatively low Vp/Vs (1.68 ± 0.04) that implies a more felsic

417   composition, although mantle upwelling generated by the combined effects of a plume, SDU (shear driven

418   upwelling) and EDC (edge driven convection) (Rawlinson et al., 2017) would likely yield melts of a mafic

419   composition, so the low Vp/Vs may be caused by something else.

420   Despite the fact that crustal composition was possibly altered by recent deformational events that resulted from

421   the break-up between Antarctica and Australia, similar Vp/Vs measurements are generally observed from the

422   southern tip of Victoria through King Island to northwestern Tasmania. This suggests a tectonic relationship

423   between northwest Tasmania and the Selwyn block and appears to support the presence of a coherent

424   Precambrian microcontinental block (VanDieland) postulated by several studies in the preceding ~20 years

425   (Cayley et al., 2002; Cayley, 2011; Moresi et al., 2014; Pilia et al., 2015a).

426   **8 Conclusions**

427   We used H-κ stacking of teleseismic RFs to determine crustal thickness and Vp/Vs ratios; we also generate 1-D

428   S-wave velocity profiles of the crust from 1-D RF inversion in order to investigate the internal crustal velocity

429   structure beneath the southern Tasmanides. We were able to verify the presence of several crustal structures

430   imaged by previous studies (Clitheroe et al., 2000; Finlayson et al., 2002; Glen et al., 2002; Reading et al., 2011;

431   Fontaine et al., 2013a,b) where there is overlap and we have also been able to provide new estimates of crustal

432   thickness and composition. We have also been able to shed fresh light on the different tectonic blocks that

433   constitute southeast Australia. The major conclusions are as follows:

434   •   The thick crust and broad crust-mantle transition beneath the Lachlan Fold Belt may be caused by
435   magmatic underplating of mafic materials beneath the crust, which is consistent with a relatively high
436   Poisson's ratio (0.262 ± 0.014). Thicker crust is also to be expected from the elevated topography
437   beneath the eastern Lachlan Fold Belt.

438   •   The crustal structure is complex in VanDieland. It thins from the northern tip of the microcontinent
439   into Bass Strait, yet in southern Tasmania the crust is thicker (33.5 ± 1.9 km) compared to Bass Strait.
440   This scenario may be attributed to the break-up of Antarctica and Australia and the opening of the
441   Tasman Sea which formed three failed rift basins that contain thick piles of sedimentary rocks (Gaina
442   et al., 1998). The thinner crust beneath Bass Strait may indicate that the thinning of the lithosphere is
443   associated with processes such as delamination and/or stretching of the lithosphere during the break-up
444   of the two continents.

445   •   Stations at ETT+EB collectively indicate crust of uniform thickness (∼33 km) and an intermediate
446   Moho transition which possibly reflects underplating associated with a Palaeozoic subduction system.

447   •   It is clear that the nature of velocity anomalies differ between stations on mainland Australia and
448   Tasmania. This highlights contrasting lithospheric structure across Bass Strait (∼ 40°S) with thin
449   lithosphere to the south and thick lithosphere to the north. This sharp transition of lithospheric
450   thickness is in agreement with previous results (Clitheroe et al., 2000) and corresponds to changes in
451   fast S-wave polarization directions from primarily northeast-southwest orientations in the north to
452   nearly northwest-southeast directions in the south (Heintz and Kennett, 2005; Pilia et al., 2016; Bello et
453   al., 2019a).

454   Results from this study advance our understanding of the nature and composition of different tectonic blocks
455   that constitute the geology of the southern Tasmanides. These results will also be important for helping to
456   understand the results from other comparable seismic imaging studies and the interpretation of tectonic
457   processes on a wider scale.

458   **9 Data availability**

459   Dataset available at 10.6084/m9.figshare.12233723

460

461   **10 Author contributions**

462   M.B. performed the data analysis and wrote the draft manuscript. N.R and D.C. guided the study and assisted in
463   interpretation. M.B., D.C. and N.R. discussed the results and revised the manuscript. A.R. and O.L. revised the
464   manuscript and assisted with the interpretation.

465   **11 Competing Interests:** The authors declare no competing interests.

466   **12 Acknowledgments**

476

477

478

479

480

481

482

483

484

485

486

487

488

489

490

491

492

493

References

494 **References**

495 Amante, C. and Eakins, B. W.: ETOPO1 1 Arc-Minute Global Relief Model: Procedures, data sources and
496   analysis, NOAA technical memorandum NESDIS NGDC-24, 19pp, 2009.

497 Ammon, C. J.: The isolation of receiver effects from teleseismic P waveforms. Bull. Seis. Soc. Ame., 81, 2504–
498   2510, 1991.

499 Ammon, C. J., Randall, G., and Zandt, G.: On the nonuniqueness of receiver function inversions. J. Geophys.
500   Res., 95, 15 303–15 318, 1990.

501 Arroucau, P., Rawlinson, N., and Sambridge, M.: New insight into Cainozoic sedimentary basins and
502   Palaeozoic suture zones in southeast Australia from ambient noise surface wave tomography. Geophys. Res.
503   Lett., 37, http://dx.doi.org/10.1029/2009GL041974, 2010.

504 Bannister, S., Yu, J., Leitner, B., and Kennett, B. L. N.: Variations in crustal structure across the transition from
505   West to East Antarctica, Southern Victoria Land, Geophys. J. Int., 155, 870–884, 2003.

506 Bello, M., Cornwell, D. G., Rawlinson, N., and Reading, A. M.: Insights into the structure and dynamics of the
507   upper mantle beneath Bass Strait, southeast Australia, using shear wave splitting, Phys. Earth Planet. Inter.,
508   289, 45–62, https://doi.org/10.1016/j.pepi.2019.02. 002, 2019a.

509 Bello, M., Rawlinson, N., Cornwell, D. G., Crowder, E., Salmon, M., and Reading, A. M.: Structure of the crust
510   and upper mantle beneath Bass Strait, southeast Australia, from teleseismic body wave tomography, Phys.
511   Earth Planet. Inter., 294, https://doi.org/10.1016/j.pepi. 2019.106276, 2019b.

512 Berry, R. F., Steele, D. A., and Maffre, S.: Proterozoic metamorphism in Tasmania: implications for tectonic
513   reconstructions, Prec. Res., 166, 387–396. https://doi.org/10.1016/j. precamres.2007.05.004, 2008.

514 Bodin, T., Salmon, M., Kennett, B. L. N., and Sambridge, M.: Probabilistic surface reconstruction from multiple
515   datasets: an example for the Australian Moho, J. Geophys. Res.: Solid Earth, 117,
516   http://dx.doi.org/10.1029/2012JB009547, 2012a.

517 Bodin, T., Sambridge, M., Rawlinson, N., and Arroucau, P.: Transdimensional tomography with unknown data
518   noise, Geophys. J. Int., 189, 1536–1556, 2012b.

519 Boger, S. and Miller, J.: Terminal suturing of Gondwana and the onset of the Ross Delamerian Orogeny: the
520   cause and effect of an Early Cambrian reconfiguration of plate motions, Earth Planet. Sci. Lett., 219, 35–48,
521   2004.

522 Calvert, C. R. and Walter, M. R.: The Late Neoproterozoic Grassy Group of King Island, Tasmania: correlation
523   and palaeogeographic significance, Precam. Res., 100, 299–312, 2000.

524 Cawood, P. A.: Terra Australis Orogen: Rodinia breakup and development of the Pacific and Iapetus margins of
525   Gondwana during the Neoproterozoic and Palaeozoic. Earth-Science Reviews, 69, 249–279,
526   http://dx.doi.org/10.1016/j.earscirev.2004.09.001, 2005.

527 Cayley, R.: Exotic crustal block accretion to the eastern Gondwanaland margin in the Late Cambrian Tasmania,
528   the Selwyn Block, and implications for the Cambrian–Silurian evolution of the Ross, Delamerian, and
529   Lachlan orogens. Gond. Res., 19, 628–649. http://dx.doi.org/10. 1016/j.gr.2010.11.013, 2011.

530 Cayley, R., Korsch, R. J., Moore, D. H., Costelloe, R. D., Nakamura, A., Willman, C. E., Rawlin, T. J., Morand,
531   V. J., Skladzien, P. B., and O'Shea, P. J.: Crustal architecture of central Victoria: results from the 2006 deep
532   crustal reflection seismic survey, Aust. J. Earth Sci., 59, 113–156, 2011.

533 Cayley, R., Taylor, D. H., VandenBerg, A. H. M., and Moore, D. H.: Proterozoic–Early Palaeozoic rocks and
534   the Tyennan Orogeny in central Victoria: the Selwyn Block and its tectonic implications, Aust. J. Earth Sci.,
535   49, 225-254, 2002.

536 Chen, Y., Niu, F., Liu, R., Huang, Z., Tkalčić, H., Sun, L., and Chan, W.: Crustal structure beneath China from
537   receiver function analysis, J. Geophys. Res., 49(B033067), 2010.

538 Chevrot, S. and van der Hilst, R. D.: The Poisson ratio of the Australian crust: Geological and Geophysical
539   implications, Earth Planet. Sci. Lett., 183,121–132, 2000.

540 Christensen, N. I.: Poisson's ratio and crustal seismology, J. Geophys. Res., 101, 3139–3156, 1996.

541 Christensen, N. I. and Fountain, D. M.: Constitution of the lower continental crust based on experimental
542   studies of seismic velocities in granulite, Geol. Soc. Ame. Bull., 86, 227–236, 1975.

543 Clitheroe, G., Gudmundsson, O., and Kennett, B.: The crustal thickness of Australia, J. Geophys. Res., 105, 13
544   697–13 713, 2000.

545 Collins, C. D. N.: The nature of crust–mantle boundary under Australia from seismic evidence, In: Drummond
546   B. J. ed. The Australian lithosphere, Geol. Soc. Aust. Spec. Pub., 17, 67–80, 1991.

547 Collins, C. D. N., Drummond, B. J., and Nicoll, M. G.: Crustal thickness patterns in the Australian continent,
548   Geol. Soc. Ame. Spec. Papers, 372, 121–128, 2003.

549 Collins, W. J.: Nature of extensional accretionary origins, Tectonics, 21, 1024–1036, 2002.

550 Collins, W. J. and Vernon, R. H.: A rift–drift–delamination model of continental evolution: Palaeozoic tectonic
551   development of eastern Australia, Tectonophysics, 2(35), 1994.

552 Coney, P. J.: Plate tectonics and the Precambrian Phanerozoic evolution of Australia, PACRIM '95, Aust. Inst.
553   Mining and Metallurgy, pages 145–150, 1995.

554 Coney, P. J., Edwards, A., Hine, R., Morrison, F., and Windrim, D.: The regional tectonics of the Tasman
555   orogenic system, eastern Australia, J. Struct. Geol., 12(5/6), 519–543, 1990.

556 Crowder, E., Rawlinson, N., Pilia, S., Cornwell, D. G., and Reading, A. M.: Transdimensional ambient noise
557   tomography of Bass Strait, southeast Australia, reveals the sedimentary basin and deep crustal structure
558   beneath a failed continental rift, Geophys. J. Int., 217, 970–987, 2019.

559 Davies, D. R., Rawlinson, N., Iaffaldano, N., and Campbell, I. H.: Lithospheric controls on magma composition
560   along Earth's longest continental hotspot track, Nature, 525, 511–514, 2015.

561 Direen, N. G., Lyons, P., Korsch, R. J., and Glen, R. A.: Integrated geophysical appraisal of crustal architecture
562   in the Eastern Lachlan Orogen, Explo. Geophys., 32, 252–262, 2001.

563 Drummond, B. J. and Collins, C. D. N.: Seismic evidence for underplating of the lower continental crust of
564   Australia, Earth Planet. Sci. Lett., 79, 361–372, 1986.

565 Drummond, B. J., Lyons, P., Goleby, B., and Jones, L.: Constraining models of the tectonic setting of the giant
566   Olympic Dam iron-oxide-copper-gold deposit, south Australia, using deep seismic reflection data,
567   Tectonophysics, 420, 91–103, 2006.

568 Eagar, K. C. and Fouch, M. J.: FuncLab: A MATLAB interactive toolbox for handling receiver function
569   datasets, Seismo. Res. Lett., https://doi.org/10.1785/gssrl.83.3.596, 2012.

570 Finlayson, D. M., Collins, C. D. N., and Denham, D.: Crustal structure under the Lachlan Fold Belt,
571   southeastern Australia, Phys. Earth Planet. Int., 21, 321–342, 1980.

572 Finlayson, D. M., Korsch, R. J., Glen, R. A., Leven, J. H., and Johnstone, D. W.: Seismic imaging and crustal
573   architecture across the Lachlan transverse zone, a crosscutting feature of eastern Australia, Aust. J. Earth
574   Sci., 49, 311–321, 2002.

575 Fishwick, S. and Rawlinson, N.: 3–D structure of the Australian lithosphere from evolving seismic datasets,
576   Aust. J. Earth Sci., 59, 809–826, 2012.

16

Solid Earth
Discussions
Open Access
EGU

577   Foden, J., Elburg, M. A., Dougherty-Page, J., and Burtt, A.: The timing and duration of the Delamerian
578   Orogeny: correlation with the Ross Orogen and implications for Gondwana assembly, J. Geology, 114, 189–
579   210, 2006.

580   Fontaine, F. R., Tkalčić, H., and Kennett, B. L. N.: Crustal complexity in the Lachlan Orogen revealed from
581   teleseismic receiver functions, Aust. J. Earth Sci., 60, 413–430, 2013a.

582   Fontaine, F. R., Tkalčić, H., and Kennett, B. L. N.: Imaging crustal structure variation across southeastern
583   Australia, Tectonophysics, 582, 112–125, 2013b.

584   Foster, D. A. and Gray, D. R.: Evolution and structure of the Lachlan Fold Belt (Orogen) of eastern Australia,
585   Annu. Rev. Earth Planet. Sci., 28, 47–80, 2000.

586   Gaina, C., Müller, D., Royer, J. Y., Stock, J., Hardebeck, J., and Symonds, P.: The tectonic history of the
587   Tasman Sea, a puzzle with 13 pieces, J. Geophys. Res., 103,12,413–12,433,1998.

588   Gibson, G. M., Morse, M. P., Ireland, T. R., and Nayak, G. K.: Arc-continent collision and orogenesis in
589   western Tasmanides: insights from reactivated basement structures and formation of an ocean-continent
590   transform boundary off western Tasmania, Gondwana Res., 19, 608–627, 2011.

591   Glen, R. A.: The Tasmanides of Eastern Australia. In: Vaughan, A. P. M., Leat, P. T., Pankhurst, R. J. (Eds.),
592   Terrane Processes at the Margins of Gondwana, Geological Society, pages 23–96, 2005.

593   Glen, R. A.: Refining accretionary orogen models for the Tasmanides of eastern Australia, Aust. J. Earth Sci.,
594   60, 315–370, 2013.

595   Glen, R. A., Korsch, R. J., Direen, N. G., Jones, L. E. A., Johnstone, D. W., Lawrie, K. C., Finlayson, D. M.,
596   and Shaw, R. D.: Crustal structure of the Ordovician Macquarie Arc, eastern Lachlan Orogen, based on
597   seismic–reflection profiling, Aust. J. Earth Sci., 49, 323–348, 2002.

598   Glen, R. A., Percival, I. G., and Quinn, C. D.: Ordovician continental margin terranes in the Lachlan Orogen,
599   Australia: implications for tectonics in an accretionary orogen along the east Gondwana margin, Tectonics,
600   28, https://doi.org/:10.1029/2009TC002446, 2009.

601   Goldstein, P., Dodge, D., Firpo, M., and Minner, L.: SAC2000: Signal processing and analysis tools for
602   seismologists and engineers. Lee, W. H. K. and Kanamori, H. and Jennings, P. C. and Kisslinger, C. (Eds.).
603   In IASPEI International Handbook of Earthquake and Engineering Seismology, Academic Press, London,
604   2003.

605   Gouveia, W. P. and Scales, J. A.: Bayesian seismic waveform inversion: Parameter estimation and uncertainty
606   analysis, J. Geophys. Res., 103, 2759–2779, 1998.

607   Gray, D. R. and Foster, D. A.: Tectonic evolution of the Lachlan Orogen, southeastern Australia: historical
608   review, data synthesis and modern perspectives, Aust. J. Earth Sci., 51, 773– 817, 2004.

609   Gunn, P. J., Maidment, D. W., and Milligan, P.: Interpreting aeromagnetic data in areas of limited outcrop,
610   AGSO J. Aust. Geol. Geophys., 17, 175–185, 1997.

611   Harrington, B. et al (2004-2005). Inkscape. http://www.inkscape.org/.

612   Haskell, N. A.: The dispersion of surface waves in multilayered media, Bulletin of the Seismological Society
613   America, 43, 1734, http://dx.doi.org/10.1038/physci245109a0, 1953.

614   He, C. S., Santosh, M., Dong, S. W., and Wang, S. C.: Crustal thickning and uplift of the Tibetan Plateau
615   inferred from receiver function analysis, J. Asian Earth Sci., 99,112–124, 2015.

616   Heintz, M. and Kennett, B. L. N.: Continental scale shear wave splitting analysis: Investigation of seismic
617   anisotropy underneath the Australian continent, Earth Planet. Sci. Lett., 236, 106–119, 2005.

618   Kennett, B. L. N. and Furumura, T.: Stochastic waveguide in the lithosphere: Indonesian subduction zone to

Solid Earth
Discussions

619   Australian craton, Geophys. J. Int., 172, 363–382, 2008.

620   Kennett, B. L. N., Salmon, M., Saygin, E., and Group, A.: AusMoho: the variation of Moho depth in Australia,
621   Geophys. J. Int., 187, 946–958, 2011.

622   Korsch, R. J., Barton, T. J., Gray, D. R., Owen, A. J., and Foster, D. A.: Geological interpretation of a deep
623   seismic reflection transect across the boundary between the Delamerian and Lachlan Orogens, in the vicinity
624   of the Grampians, western Victoria, Aust. J. Earth Sci., 49, 1057–1075, http://dx.doi.org/10.1046/j.1440-
625   0952.2002.00963.x, 2002.

626   Langston, C. A.: Structure under Mount Rainier, Washington, inferred from teleseismic body waves, J.
627   Geophys. Res., 84, 4749–4762, https://doi.org/10.1071/EG994019, 1979.

628   Li, Z. X., Baillie, P. W., and Powell, C. M.: Relationship between northwestern Tasmania and East
629   Gondwanaland in the Late Cambrian/Early Ordovician Paleomagnetic evidence, Tectonics, 16, 161–171,
630   http://dx.doi.org/10.1029/96TC02729, 1997.

631   Ligorria, J. P. and Ammon, C. J.: Iterative deconvolution and receiver function estimation, Bull. Seism. Soc.
632   Ame., 89, 1395–1400, 1999.

633   Mavko, M.: Velocity and attenuation in partially molten rocks, J. Geophys. Res., 85, 5173–5189,
634   https://doi.org/10.1029/JB085iB10p05173, 1980.

635   Moore, D., Betts, P. G., and Hall, M.: Fragmented Tasmania: the transition from Rodinia to Gondwana, Aust. J.
636   Earth Sci., 62, 1–35, 2015.

637   Moore, D. H., Betts, P. G., and Hall, M.: Constraining the VanDieland microcontinent at the edge of East
638   Gondwana, Australia, Tectonophysics, 687, 158–179, 2016.

639   Moresi, L., Betts, P. G., Miller, M. S., and Cayley, R. A.: Dynamics of continental accretion, Nature, 508, 245–
640   248, 2014.

641   Morse, M., Gibson, G., and Mitchell, C.: Basement constraints on offshore basin architecture as determined by
642   new aeromagnetic data acquired over Bass Strait and western margin of Tasmania, ASEG Extended
643   Abstracts 2009, pages 1–9, http://dx.doi.org/10.1071/ASEG2009ab042, 2009.

644   Owens, T. J., Taylor, S. R., and Zandt, G.: Crustal structure at regional seismic test network stations determined
645   from inversion of broadband teleseismic P waveforms, Bull. Seismo. Soc. Ame., 77, 631–632, 1987.

646   Owens, T. J. and Zandt, G.: Implications of crustal property with variations for models of Tibetan Plateau
647   evolution, Nature, 387, 37–43, 1997.

648   Pan, S. Z. and Niu, F. L.: Large contrasts in crustal structure and composition between the Ordos plateau and the
649   NE Tibetan plateau from receiver function analysis, Earth Plan. Sci. Lett., 303, 291–298, 2011.

650   Pilia, S., Arroucau, P., Rawlinson, N., Reading, A. M., and Cayley, R. A.: Inherited crustal deformation along
651   the East Gondwana margin revealed by seismic anisotropy tomography, Geophys. Res. Lett., 43(23), 12082–
652   12090, https://doi.org/10.1002/2016GL071201, 2016.

653   Pilia, S., Rawlinson, N., Cayley, R. A., Musgrave, R., Reading, A. M., Direen, N. G., and Young, M. K.:
654   Evidence of micro–continent entrainment during crustal accretion, Sci. Rep., 5,
655   http://dx.doi.org/10.1038/srep/08218, 2015a.

656   Pilia, S., Rawlinson, N., Green, N. G., Reading, A. M., Cayley, R., Pryer, L., Arroucau, P., and Duffet, M.:
657   Linking mainland Australia and Tasmania using ambient seismic noise tomography: Implications for the
658   tectonic evolution of the east Gondwana margin, Gond. Res., 28, 1212–1227, 2015b.

659   Porritt, S. W. and Miller, M. S.: Updates to FuncLab, a Matlab based GUI for handling receiver functions,
660   Computers and Geosciences, 111, 260–271, https://doi.org/10.1016/j. cageo.2017.11.022, 2018.

Solid Earth
Discussions
Open Access
EGU

661   Rawlinson, N., Davies, D. R., and Pilia, S.: The mechanisms underpinning Cenozoic intraplate volcanism in
662   eastern Australia, Insights from seismic tomography and geodynamic modeling, Geophys. Res. Lett., 44(19),
663   9,681–9,690, 2017.

664   Rawlinson, N., Housman, G. A., Collins, C. D. N., and Drummond, B. J.: New evidence of Tasmania's tectonic
665   history from a novel seismic experiment, Geophys. Res. Lett., 28, 3337–3340, 2001.

666   Rawlinson, N. and Kennett, B.: Teleseismic tomography of the upper mantle beneath the southern Lachlan
667   Orogen, Australia, Phys. Earth Planet. Inter., 167, 84–97, http://dx.doi.org/ 10.1016/j.pepi2008.02.07, 2008.

668   Rawlinson, N., Kennett, B., Vanacore, E., Glen, R., and Fishwick, S.: The structure of the upper mantle beneath
669   the Delamerian and Lachlan orogens from simultaneous inversion of multiple teleseismic datasets, Gond.
670   Res., 19, 788–799, 2011.

671   Rawlinson, N., Kennett, B. L. N., Salmon, M., and Glen, R. A.: Origin of lateral heterogeneities in the upper
672   mantle beneath Southeast Australia from seismic tomography, Khan, A., and Deschamps, F. (Eds.), In The
673   Earth's Heterogeneous Mantle: A Geophysical, Geodynamical and Geochemical Perspective, pages 47–78,
674   Springer Geophysics, Springer, 2015.

675   Rawlinson, N., Pilia, S., Young, M., Salmon, M., and Yang, Y.: Crust and upper mantle structure beneath
676   southeast Australia from ambient noise and teleseismic tomography, Tectonophysics, 689, 143–156,
677   http://dx.doi.org/10.1016/j.tecto.2015.11.034, 2016.

678   Rawlinson, N., Pozgay, S., and Fishwick, S.: Seismic tomography: a window into deep Earth, Phys. Earth
679   Planet. Inter., 178, 101–135, 2010.

680   Rawlinson, N. and Urvoy, M.: Simultaneous inversion of active and passive source datasets for 3–D seismic
681   structure with application to Tasmania, Geophys. Res. Lett., 33, 2006.

682   Reading, A. M., Tkalčić, H., Kennett, B. L. N., Johnson, S. P., and Sheppard, S.: Seismic structure of the crust
683   and uppermost mantle of the Capricon and Paterson Orogens and adjacent cratons, Western Australia, from
684   passive seismic transects, Prec. Res., 196–197, 295–308, 2011.

685   Sambridge, M. S.: Geophysical inversion with a neighbourhood algorithm – I. Searching a parameter space,
686   Geophys. J. Int., 138, 479–494, 1999a.

687   Sambridge, M. S.: Geophysical inversion with a neighbourhood algorithm -II. Appraising the ensemble,
688   Geophys. J. Int., 138, 479–494, 1999b.

689   Saygin, E. and Kennett, B. L. N.: Ambient seismic noise tomography of Australian continent, Tectonophysics,
690   481, 116–125, http://dx.doi.org/10.1016/j.tecto.2008.11.013, 2010.

691   Shibutani, T., Sambridge, M. S., and Kennett, B. L. N.: Genetic algorithm inversion for receiver functions with
692   application to crust and uppermost mantle structure beneath Eastern Australia, Geophys. Res. Lett.,
693   23,1826–1832, 1996.

694   Spaggiari, C. V., Gray, D. R., and Foster, D. A.: Lachlan Orogen subduction–accretion systematics revisited,
695   Aust. J. of Earth Sci., 51, 549–553, 2004.

696   Spaggiari, C. V., Gray, D. R., Foster, D. A., and McKnight, S.: Evolution of the boundary between the western
697   and central Lachlan Orogen: implications for Tasmanide tectonics, Aust. J. Earth Sci., 50, 725–749, 2003.

698   Teasdale, J., Pryer, L., Stuart-Smith, P., Romine, K., Etheridge, M., Loutit, T., and Kyan, D.: Structural
699   framework and basin evolution of Australia's Southern Margin, APPEA J. Australian Petroleum Production
700   and Exploration Association, 43, 13–38, https://doi.org/10. 1785/0120030123, 2003.

701   Thomson, W. T.: Transmission of elastic waves through a stratified solid, J. of App. Phys., 21, 89-93, 1950.

702   Tkalčić, H., Chen, Y., Liu, R., Huang, H., Sun, L., and Chan, W.: Multi–step modelling of teleseismic receiver
703   functions combined with constraints from seismic tomography: Crustal structure beneath southeast China,

Solid Earth
Discussions
Open Access
EGU

704   Geophys. J. Int., 187, 303–326, 2011.

705   Tkalčić, H., Rawlinson, N., Arroucau, P., and Kumar, A.: Multistep modelling of receiver-based seismic and
706   ambient noise data from WOMBAT array: crustal structure beneath southeast Australia, Geophys. J. Int.,
707   189, 1681–1700, https://doi.org/10.1111/j.1365-246X.2012.05442, 2012.

708   Wessel, P., Smith, W. H., Scharroo, R., Louis, J., and Wobbe, F.: Generic mapping tools: improved version
709   released, EOS Trans. Am. Geophys. Union, 94, 409-420, 2013.

710   White, L., Gibson, G., and Lister, G.: A reassessment of paleogeographic reconstructions of eastern Gondwana:
711   bringing geology back into the equation, Gond. Res., 24, 984–998, http:
712   //dx.doi.org/10.1016/j.gr.2013.06.00, 2013.

713   Young, M. K., Cayley, R. A., McLean, M. A., Rawlinson, N., Arroucau, P., and Salmon, M.: Crustal structure
714   of the east Gondwana margin in southeast Australia revealed by transdimensional ambient seismic noise
715   tomography, Geophys. Res. Lett., 40, 4266–4271, 2013a.

716   Young, M. K., Cayley, R. A., McLean, M. A., Rawlinson, N., Arroucau, P., and Salmon, M.: Crustal structure
717   of the east Gondwana margin in southeast Australia revealed by transdimensional ambient seismic noise
718   tomography, Geophys. Res. Lett., 40, 4266–4271, 2013b.

719   Young, M. K., Rawlinson, N., Arroucau, P., Reading, A., and Tkalčić, H.: High–frequency ambient noise
720   tomography of southeast Australia: new constraints on Tasmania's tectonic past, Geophys. Res. Lett., 38,
721   http://dx.doi.org/10.1029/2011GL047971, 2011.

722   Young, N., Tkalčić, H., Rawlinson, N., and Reading, A. M.: Full waveform moment tensor inversion in a low
723   seismicity region using multiple teleseismic datasets and ambient noise: application to the 2007 Shark Bay,
724   Western Australia, Earthquake. Geophys. J. Int., 188,1303–1321, https://doi.org/10.1111/j.1365-
725   246X.2011.05326, 2012.

726   Zhu, L. and Kanamori, H.: Moho depth variation in southern California from teleseismic receiver functions, J.
727   Geophys. Res., 105, 2969–2980, 2000.

728

729

730

731

732

733

734

735

736

737

738

739

740

741

742

743

744

745

Solid Earth
Discussions

Open Access

EGU

746

747

748

749

750

751

Table 1: Model parameter bounds used in the Neighbourhood Algorithm receiver function inversion. V_s^{upper} and V_s^{lower} represent the S-velocity at the top and bottom of a layer respectively. V_p/V_s represents P and S wave velocity ratio within a layer.

Layer	Thickness (m)	V_s^{upper} (km/s)	V_s^{lower} (km/s)	V_p/V_s
Sediment	0-2	0.5-1.5	0.5-1.5	2.00-3.00
Basement	0-3	1.8-2.8	1.8-2.8	1.65-2.00
Upper crust	3-20	3.0-3.8	3.0-3.9	1.65-1.80
Middle crust	4-20	3.4-4.3	3.4-4.4	1.65-1.80
Lower crust	5-15	3.5-4.8	3.6-4.9	1.65-1.80
Mantle	5-20	4.0-5.0	4.0-5.0	1.70-1.90

752

753

754

755

756

757

758

759

760

761

762

763

764

765

766

Table 2: Moho depth, V_p/V_s, Poisson's ratio and nature of the Moho for siesmic stations analysed by two different techniques used in this study.

| | Basic station information | | | | Results | | | | |
Name	No. of RFs	Lon.(°)	Lat.(°)	Moho depth grid search	Moho depth inversion	Quality inversion	Bulk V_p/V_s	Poisson's ratio (σ)	Nature
VanDieland									
BA02	4	145.20	-40.95	31.4±2.1	-	-	1.69±0.02	0.231±0.017	-
BA11	12	143.98	-39.64	30.5±2.1	-	-	1.65±0.07	0.210±0.013	-
TAU	41	147.32	-42.91	33.5±1.9	33	poor	1.70±0.08	0.235±0.036	intermediate
MOO	58	147.19	-42.44	33.0±1.2	34	good	1.71±0.04	0.240±0.019	sharp
TOO	276	145.59	-37.57	37.5±1.2	35	good	1.68±0.04	0.226±0.017	sharp
Lachlan Fold Belt									
YNG	178	148.40	-34.30	37.0±1.2	48	good	1.76±0.04	0.262±0.014	broad
CAN	402	149.00	-35.32	39.1±0.5	49	very good	1.73±0.02	0.250±0.008	broad
CNB	155	149.36	-35.32	38.5±1.1	46	good	1.70±0.04	0.235±0.017	broad
MILA	4	149.16	-37.05	37.6±2.1	-	-	1.73±0.06	0.251±0.023	-
BA13	6	148.83	-37.63	36.5±4.4	-	-	1.72±0.12	0.245±0.045	-
ETT+EB									
BA07	5	148.31	-40.43	32.5±0.1	-	-	1.70±0.02	0.235±0.001	-
BA08	13	147.97	-39.77	34.0±1.2	-	-	1.67±0.03	0.220±0.008	-
BA17	5	146.33	-39.04	33.2±0.5	-	-	1.71±0.02	0.242±0.008	-

767

768

769

770

771
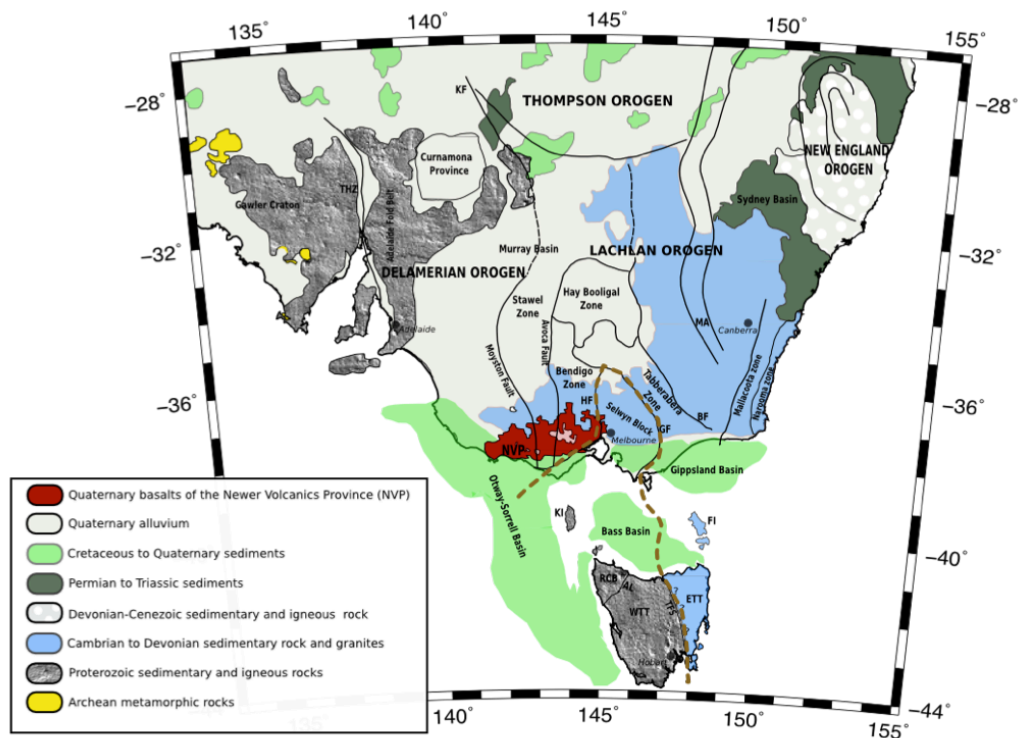
772

773

774

775

776 **Figure 1: Regional map of southeastern Australia that shows key geological boundaries and the locations of observed
777 or inferred tectonic units (Modified from Bello et al., 2019a). Thick black lines delineate structural boundaries and
778 the thick brown dashed line traces out the boundary of VanDieland. HF = Heathcote Fault; GF = Governor Fault;
779 BF = Bootheragandra Fault; KF = Koonenberry Fault; THZ = Torrens Hinge Zone; MA = Macquarie Arc; NVP =
780 Newer Volcanics Province; KI = King Island and FI = Flinders Island in Bass Strait; ETT = East Tasmania Terrane;
781 WTT = West Tasmania Terrane; TFS = Tamar Fracture System; AL = Arthur Lineament and RCB = Rocky Cape
782 Block. Outcrop boundaries are sourced from Rawlinson et al. 2016.**

783

784
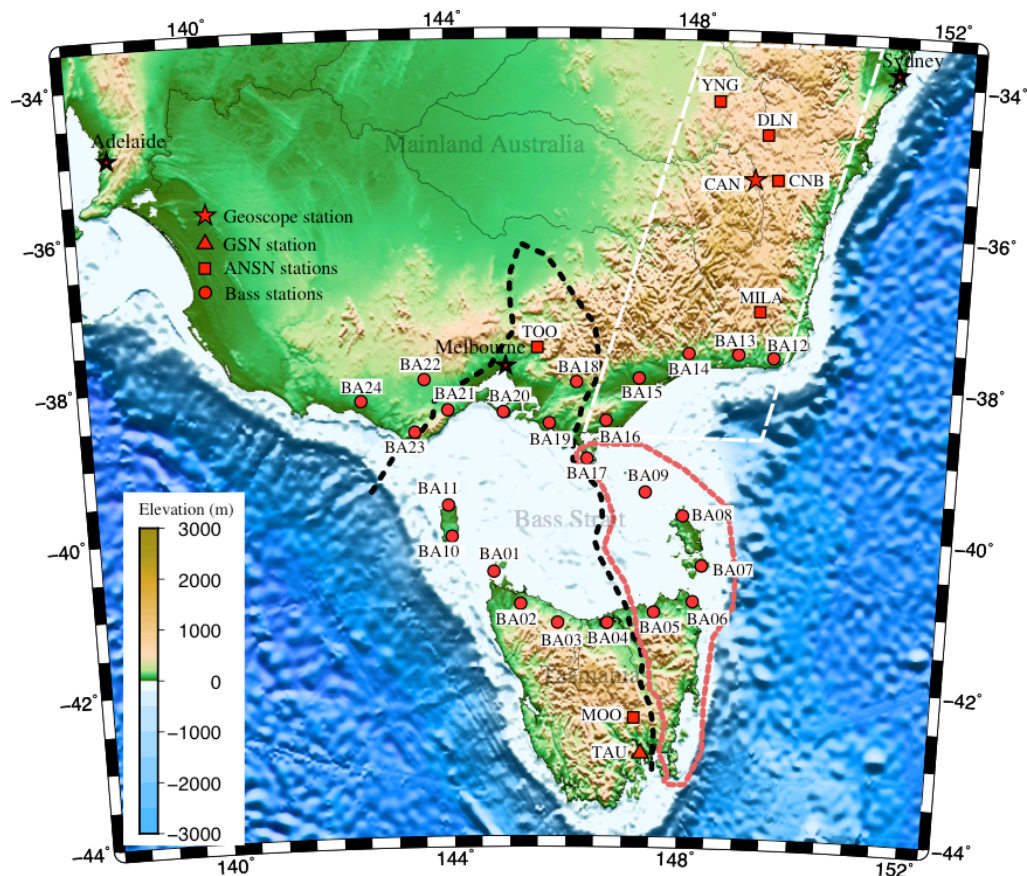
Figure 2: Location of seismic stations used in this study superimposed on a topographic/bathymetric map of southeast Australia (Modified from Bello et al., 2019a). The boundary of VanDieland is delineated by a thick black dashed line. The boundary of the East Tasmania Terrane and Furneaux Islands is represented by a thick dashed red line, while a thick dashed white line traces out the eastern sector of the Lachlan Fold Belt. Topography/bathymetry is based on the Etopo1 dataset (Amante and Eakins, 2009).
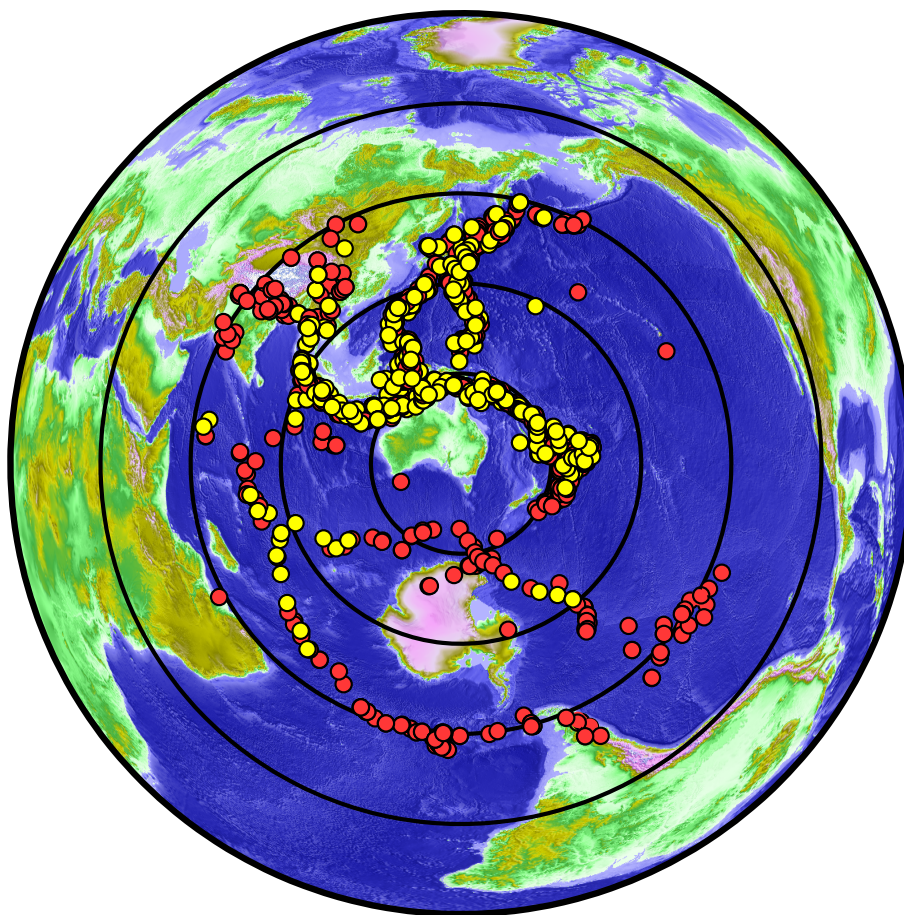
794
795
796   **Figure 3: Distribution of distant earthquakes (teleseisms) used in the study. The locations of events that are**
797   **ultimately used for RF analysis are denoted by yellow dots. Concentric circles are plotted at 30° intervals from the**
798   **centre of Bass Strait.** Topography/bathymetry is based on the Etopo1 dataset (Amante and Eakins, 2009).

799
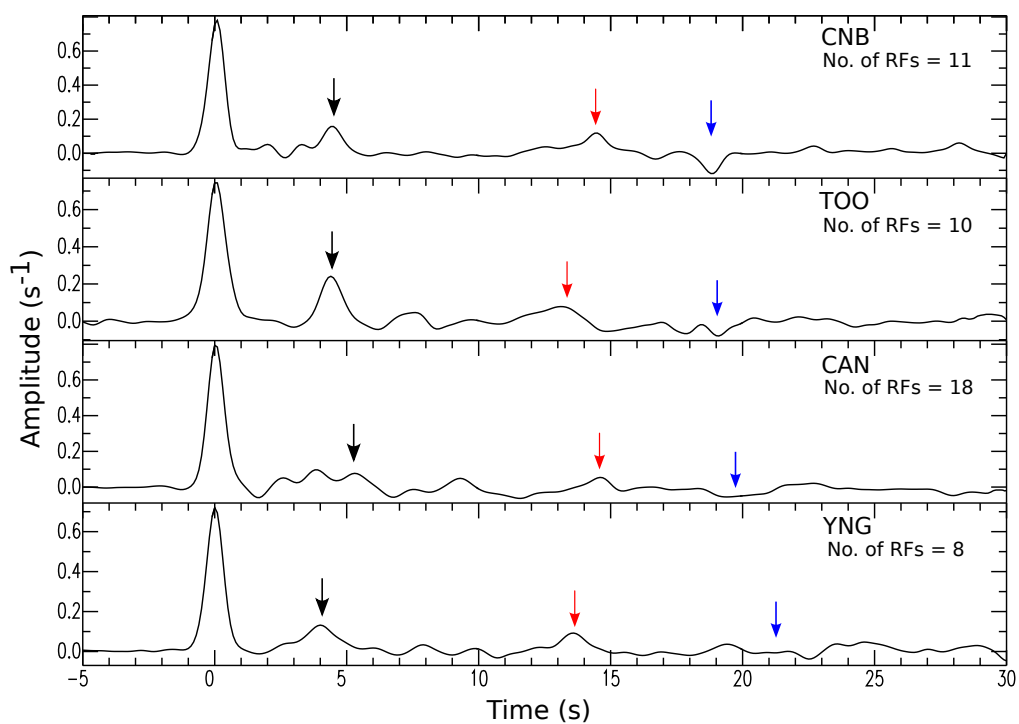
Figure 4: Stacked receiver functions from Australian National Seismic Network (ANSN) stations TOO, YNG, MOO and GSN station TAU. Small arrows indicate arrival of the *Ps* (black), *PpPs* (red) and *PpPs* + *PsPs* (blue) phases from the Moho.
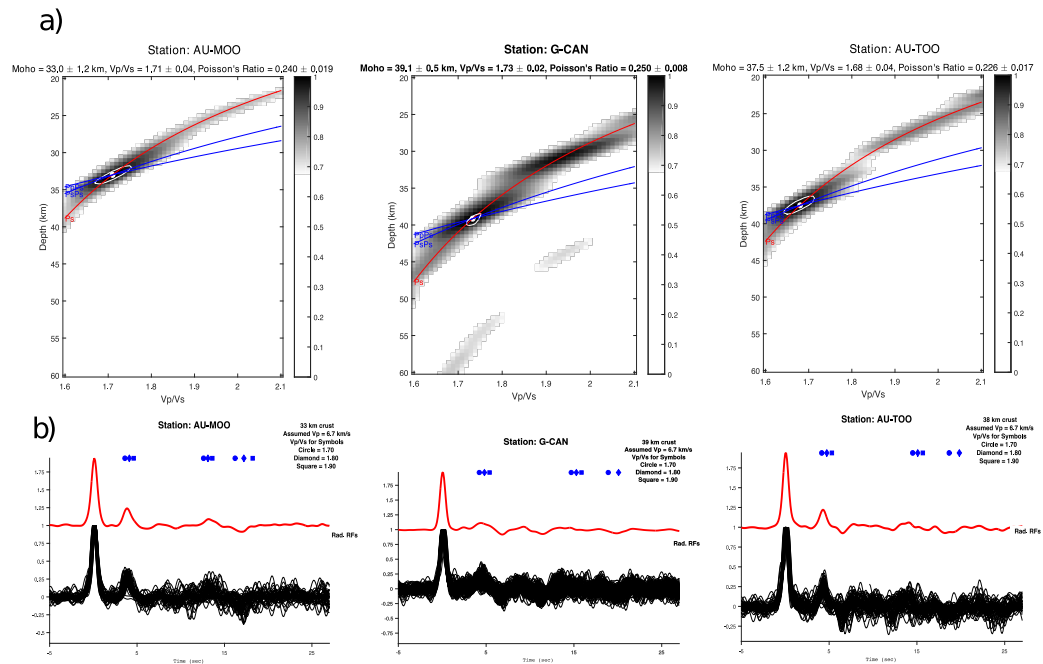
Figure 5: Results from the *H-κ* stacking analysis for RFs (Zhu and Kanamori, 2000) at stations MOO, CAN and TOO. In each case (a) Normalised amplitudes of the stack over all back-azimuths along the travel time curves corresponding to the P_S and P_pP_S phases. (b) Corresponding stacked receiver function for each station.
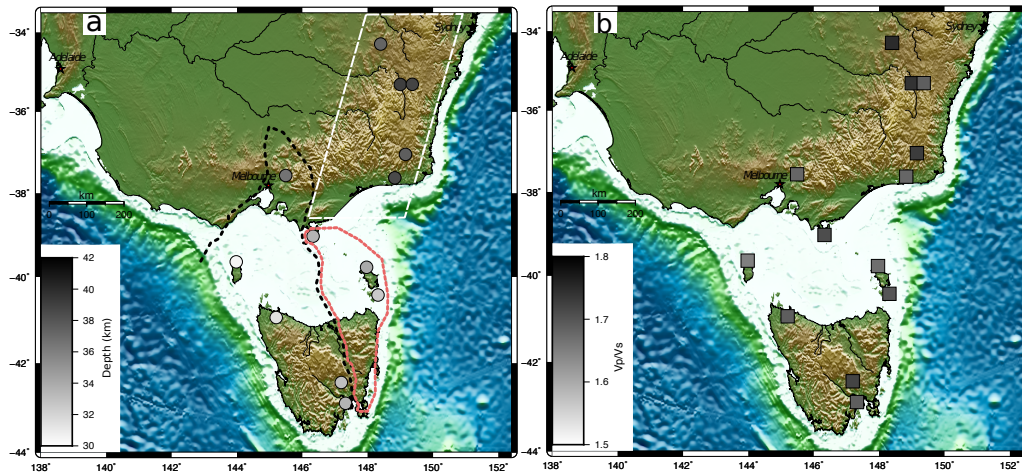
Figure 6: (a) Variations in crustal thickness and (b) V_p/V_s ratio taken from the linear (H-κ) stacking results (Table 2). Crustal thickness varies between 30.5 ± 0.1 km and 39.1 ± 0.5 km. Thinner crust in Bass Strait can be seen flanked by a relatively thicker crust to the north and south. V_p/V_s ratios vary from 1.65 ± 0.02 to 1.75 ± 0.02. Thick black dashed line denotes the boundary of VanDieland. Thick red dashed line outlines the boundary of East Tasmania Terrane and eastern Bass Strait (ETT+EB). Thick white dashed line highlights the eastern part of the Lachlan Fold Belt. Topography/bathymetry is based on the Etopo1 dataset (Amante and Eakins, 2009).

828
829
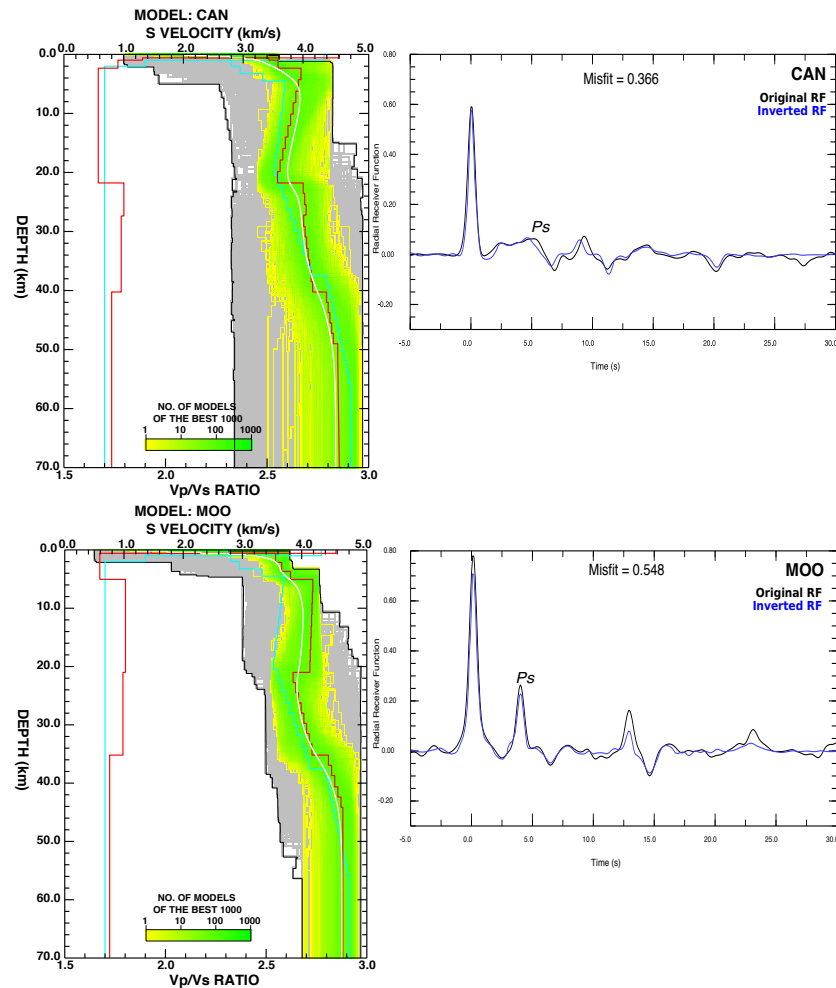
Figure 7: (Left) Seismic velocity models for CAN and MOO stations obtained from the neighbourhood algorithm (Sambridge 1999a). The grey area indicates all the models searched by the algorithm. The best 1000 models are indicated by the yellow to green colours; the best one (smallest misfit) corresponds to the red line, both for *S*-wave velocity and V_p/V_s ratio and the white line is the average velocity model. (Right) Waveform matches between the observed stacked receiver functions (black) and predictions (blue) based on the best models.

835
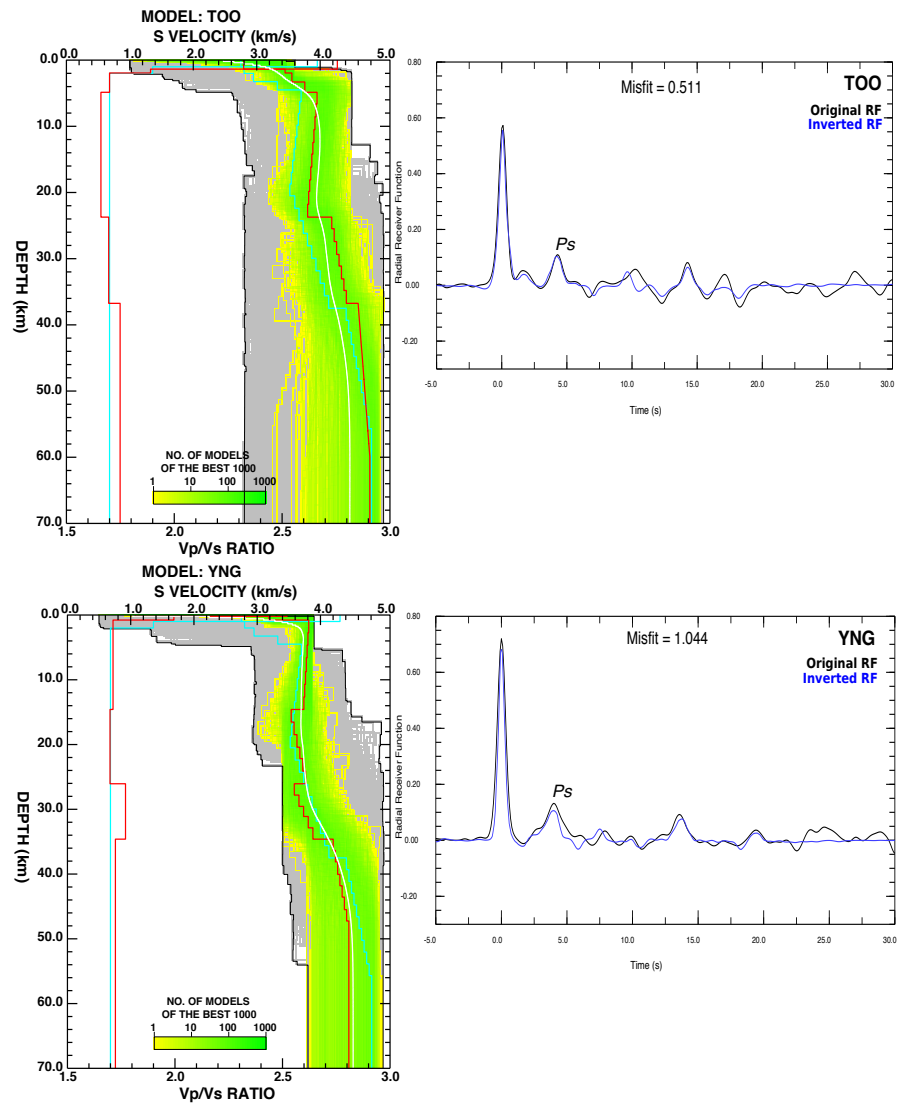
836
837
838 **Figure 8: (Left) Seismic velocity models for stations TOO and YNG obtained from the neighbourhood algorithm.**
839 **(Right) Comparison between the observed stacked and the predicted receiver functions from the NA inversion. See**
840 **Figure 7 caption for more details.**

841
842
843

30
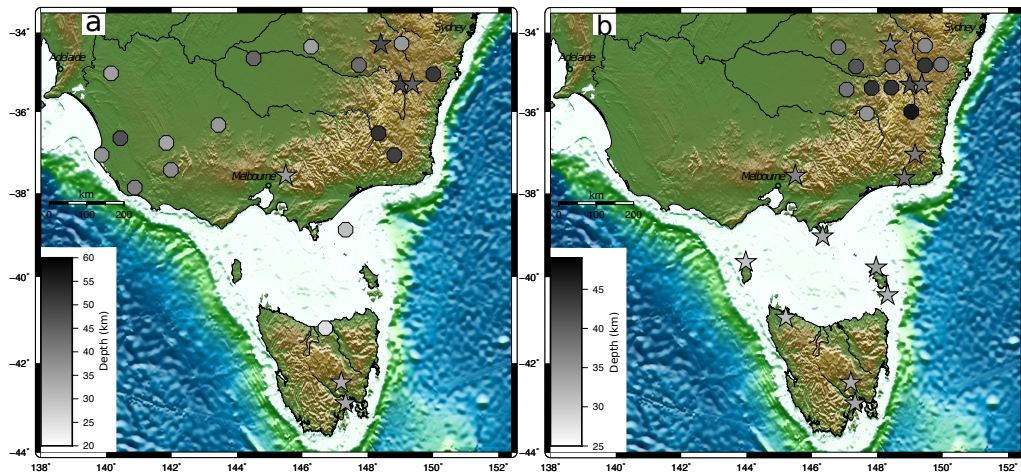
844
845

846
847 **Figure 9: (a) Map showing crustal thickness variations based on the S-wave velocity inversion results of this study**
848 **(stars) and previous studies (octagons) (Fontaine et al., 2013; Shibitani, 1996; Collins, 1991) and (b) comparison of**
849 **crustal thickness variations based on the *H-κ* grid search results of this study (stars) and previous results from the**
850 **study of Tkalčić et al. (2012) (octagons).** Topography/bathymetry is based on the Etopo1 dataset (Amante and
851 Eakins, 2009).

852
853

854

855

856

857

858

859

860

31